Visible–Light Photocatalysis in Ca0.6Ho0.4MnO3 Films Deposited by RF–Magnetron Sputtering Using Nanosized Powder Compacted Target

4 AUTHORS:

Beatriz Barrocas
University of Lisbon
7 PUBLICATIONS **25** CITATIONS

SEE PROFILE

S. Sério
New University of Lisbon
27 PUBLICATIONS **169** CITATIONS

SEE PROFILE

Ana Rovisco
New University of Lisbon
3 PUBLICATIONS **5** CITATIONS

SEE PROFILE

M. E. Melo Jorge
University of Lisbon
37 PUBLICATIONS **315** CITATIONS

SEE PROFILE

Visible-Light Photocatalysis in Ca$_{0.6}$Ho$_{0.4}$MnO$_3$ Films Deposited by RF-Magnetron Sputtering Using Nanosized Powder Compacted Target

B. Barrocas,[†] S. Sério,[‡] A. Rovisco,[‡] and M. E. Melo Jorge*,[§]

[†]Departamento de Química e Bioquímica, Faculdade de Ciências da Universidade de Lisboa, Campo Grande C8, 1749-016 Lisboa, Portugal

[‡]CEFITEC, Departamento de Física, Faculdade de Ciências e Tecnologia da Universidade Nova de Lisboa, 2829-516 Caparica, Portugal

[§]CCMM, Departamento de Química e Bioquímica, Faculdade de Ciências da Universidade de Lisboa, Campo Grande C8, 1749-016 Lisboa, Portugal

ABSTRACT: A novel immobilized Ca$_{0.6}$Ho$_{0.4}$MnO$_3$ photocatalyst has been developed with high photocatalytic activity for Rhodamine 6G (Rh6G) photodegradation under visible light irradiation. The nanocrystalline Ca$_{0.6}$Ho$_{0.4}$MnO$_3$ films were successfully deposited by RF-magnetron sputtering on unheated quartz glass substrates using Ca$_{0.6}$Ho$_{0.4}$MnO$_3$ powder as sputtering target and its photocatalytic functionalities have been explored. The visible-light-responsive photocatalytic activity of Ca$_{0.6}$Ho$_{0.4}$MnO$_3$ films was evaluated by the photodegradation of Rh6G aqueous solutions under visible light irradiation. The reusability of Ca$_{0.6}$Ho$_{0.4}$MnO$_3$ films on fresh dye samples was studied, showing an efficient reuse, without decreasing the photocatalytic decolorization efficiency. Furthermore, X-ray diffraction of the reused films did not reveal additional phases indicating high photochemical stability of the films even after reusing them in successive runs. The photocatalytic efficiency of the nanocrystalline Ca$_{0.6}$Ho$_{0.4}$MnO$_3$ films was further compared with TiO$_2$ films also produced by sputtering and the results revealed a significant improvement in photocatalytic activity over TiO$_2$ under visible light irradiation. Almost complete photodecolorization of a 5 ppm Rh6G solution was achieved in 4 h, while only 64% of dye degradation was observed in TiO$_2$ photoassisted process. This work provides a feasible route to fabricate high-performance immobilized ABO$_3$-based nanomaterials, and the finding opens up a new venue for designing visible light sensitive ternary compounds for photocatalytical applications.

Photodegradation of Rh6G under visible light
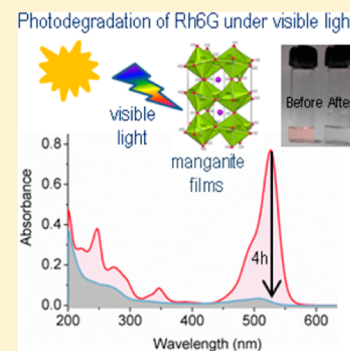
1. INTRODUCTION

In past years, photocatalysts have been extensively studied due to their potential applications in energy production and in environmental remediation. The possibility of inorganic materials to harvest and convert solar energy has been intensively explored in recent years.[1−3] There are already some metal oxides that are able to photocatalytically breakdown various water pollutants. However, the yields of these reactions continue to be low, and the majority of them occur only upon UV light irradiation. Since UV light corresponds to only approximately 4% of the incoming solar energy at the Earth's surface,[4] one of the main challenges in developing an economically viable photocatalytic material is to broaden the photocatalyst photoresponse into the visible-light region. TiO$_2$ is an important semiconductor photocatalytic material that has been extensively studied;[5−7] however, due to its wide band gap (∼3.2 eV), it is more efficient in the UV region. Consequently, it is desirable to develop photocatalytic materials that are active under visible light, since this corresponds approximately to half of all solar energy.[4]

In the past decade, several studies have been carried out in order to search for efficient photocatalysts with visible light activity by metal and/or nonmetal doping,[8,9] solid solution structures,[10,11] metal particles anchored on surfaces (i.e., noble-metal/TiO$_2$ (SrTiO$_3$),[12,13] semiconductor heterogeneous structures,[14−16] and so forth.

Over the past two decades, perovskite-based metal oxides (ABO$_3$) have been the subject of several studies due to their potential in tailoring their structure through cationic substitutions at either A or B sites and also due to the ability of tuning their optical and electrical properties, leading to a wide range of possibilities.[17] The large atoms at the A site can stabilize the active B-site transition metal ion. ABO$_3$ perovskite-type oxides contain the corner-shared octahedral BO$_6$ network, which can contribute to a high mobility of electron and oxygen and may lead to the oxygen nonstoichiometry. Moreover, the valence state of B-site transition metal ion is also crucial to the activity of perovskite-type oxides. Perovskite-type oxides have been known as an important class of multifunctional materials exhibiting a wide variety of interesting properties, such as magnetic, electronic transport, optical and dielectric properties.

Recently, the photocatalytic activity of perovskite oxides has attracted considerable attention. Among them, perovskite-type bismuth ferrite ($BiFeO_3$) shows a high potential for photocatalytic applications due to the small band gap (∼2.2−2.8 eV)[18] and good chemical stability, which makes $BiFeO_3$ an effective photocatalyst in the UV and visible light region during the photocatalytic process.[19] $LaFeO_3$ with a typical ABO_3-type perovskite structure is another potential semiconductor material as efficient visible photocatalyst due to its narrow band gap energy (2.11−2.07 eV).[20−22] Besides these compounds, the $LaMO_3$ (M = Cr, Mn, Fe, Co, Ni) and $REFeO_3$ (RE = Y, Sm, Eu, Gd) photocatalytic activity in the photodegradation of several water-soluble dyes is noteworthy.[23−25] Furthermore, it is known that the performance of materials used in photocatalytic degradation is influenced by factors like band gap energies, features associated with cation vacancy, oxygen deficiency, and surface area.[26] In addition, the relatively small band gaps exhibited by these oxides are suitable for the absorption of visible light, and thus potential candidates for efficient visible-light-responsive photocatalysts.

Most of the reactors for water treatment employ powder-type photocatalysts which have higher activity due to less mass transfer limitations between the treated contaminants and the photocatalyst. However, recovering powder-type photocatalysts from treated water is a major obstacle and requires pose-filtration treatment, which complicates the treatment procedure. Therefore to implement the photocatalysis process at industrial scale, researchers have tried to develop alternatives to anchor particles onto substrates. The immobilized nanomaterials will be prepared by RF-magnetron sputtering technique over quartz glass substrates using powders with the desired composition as sputtering target. Results achieved by utilizing this new approach for the preparation of the immobilized nanomaterials will allow an easy handling of the photocatalyst, which enables its use in more than bench tests. This technique presents several advantages such as high deposition rates, films with high purity, high adherence, and a wide industrial applicability.

In this context, this paper reports for the first time the preparation of the perovskite-type oxide $Ca_{0.6}Ho_{0.4}MnO_3$ catalyst in immobilized form by RF-magnetron sputtering using nanosized powder target previously synthetized by the citrate sol−gel method.[27,28] The material photocatalytic activity was examined on the decolorization of rhodamine 6G (Rh6G) aqueous solutions, under visible irradiation. The decomposition rate was also compared in the present work with the one exhibited by TiO_2 films, previously prepared and described in detail elsewhere,[7,29,30] for similar experimental photodegradation conditions. Rh6G is an N-containing dye, which was selected as a model pollutant in this work, since it is an important dyeing agent used in textile industries and in other applications; untreated or partially treated dyes from industries contribute to the pollution load. The dyes are complex molecules, very difficult to degrade, and very toxic; therefore the effluent water from the industries has to be treated before it is discharged in natural water stream. To test the suitability for practical applications and the stability of the perovskite-type oxides in dye aqueous solutions, the reusability of the films was also studied.

2. MATERIALS AND METHODS

All reagents were of analytical grade (Aldrich and Fluka) and were used as received. The solutions were prepared with Millipore Milli-Q ultra pure water.

2.1. Preparation of $Ca_{0.6}Ho_{0.4}MnO_3$ Films. $Ca_{0.6}Ho_{0.4}MnO_3$ films were deposited on unheated fused silica substrates by RF-magnetron sputtering using $Ca_{0.6}Ho_{0.4}MnO_3$ solid solutions as the sputtering target. The polycrystalline $Ca_{0.6}Ho_{0.4}MnO_3$ sample, used as the target, was previously prepared by the citrate nitrate self-combustion method as reported and described in detail elsewhere.[27,28] After the decomposition at 600 °C, for 6 h, the resulting amorphous powder was grounded and heated in air at 800 °C for 18 h in alumina crucibles (Alsint 99.7). The sputtering target with a diameter of 25 mm was prepared by mixing the synthesized powder with acetone. The mixture was placed on the cathode top, and it was pressed and compacted until the acetone evaporation. The cylindrical body planar magnetron cathode is a prototype that was specially developed and built in our laboratory to support powder targets with reduced diameter (25 mm) and thickness (1 mm). Figure 1 is a schematic
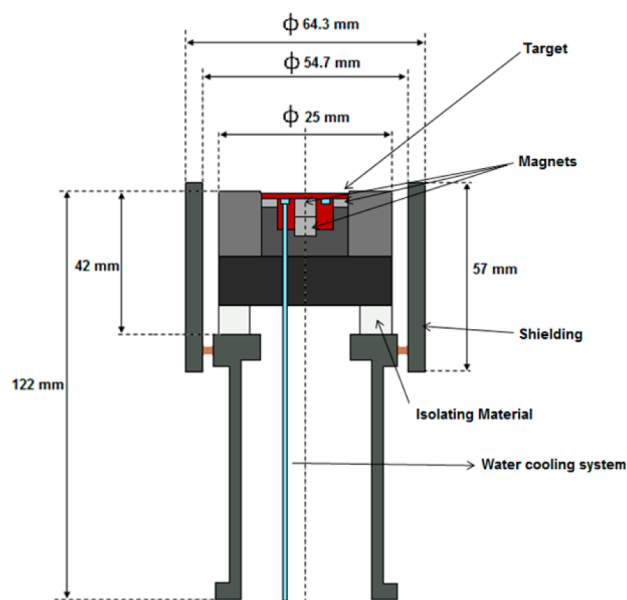
Figure 1. Schematic diagram of the magnetron cathode prototype developed and built by CEFITEC lab.

representation of the cathode prototype used to prepare the Manganite films. The magnetic circuit uses outer and inner NdFeB magnets bridged by mild steel. The magnetron cathode is installed in a cylindrical vacuum chamber pumped by a turbomolecular pump, which guarantees a pressure of 5×10^{-4} Pa in about 1 h. The target was sputtered in 99.999% pure argon at constant total sputtering gas pressure (P_{tot}) of 0.23 Pa, and the deposition time was 80 min. An RF power supply was used: Plasmaloc 2HF and the depositions were done using a sputtering power of 25 W and frequency = 100 kHz. The fused silica substrates (25 mm ×40 mm and 1 mm thick) were placed parallel to and by a distance of 20 mm toward the target. Prior to the depositions, the substrates were cleaned successively in acetone, isopropanol, and deionized water for 5 min each step and dried with nitrogen gas to remove any organic contamination. A turbomolecular pump was used to achieve a base pressure of 5×10^{-4} Pa (before introducing the sputtering

gas). Finally, the as-deposited manganites films were post-annealed at 800 °C for 6 h in air for crystallization and complete formation of the perovskite phase.

2.2. Decolorization Studies and Reuse of $Ca_{0.6}Ho_{0.4}MnO_3$ Catalysts. Rhodamine 6G (Rh6G) was used as a model contaminant to evaluate the photocatalytic behavior of the prepared thin films under visible light irradiation. The photodegradation experiments were conducted in a 250 mL refrigerated photoreactor.[7,31] A 450 W Hanovia medium-pressure mercury-vapor lamp with $0.37 W/cm^2$ of watt density, was used as the radiation source. Of the total irradiated energy, 40−48% is in the ultraviolet range and 40−43% in the visible region of the electromagnetic spectrum. In order to ensure the catalysis of the Rh6G on $Ca_{0.6}Ho_{0.4}MnO_3$ films only under visible light wavelengths, a cut-off filter was placed around the cold trap to completely remove radiation below 400 nm. To perform each catalytic photodegradation experiment, two $Ca_{0.6}Ho_{0.4}MnO_3$ films with $9.75\ cm^2$ geometric area each, performing a total area of $19.5\ cm^2$, were immersed into 175 mL of 5 ppm Rh6G aqueous solution. Before irradiation, the solutions were stirred in the absence of light for 1 h to create an equilibrium of adsorption−desorption between Rh6G and the photocatalyst. This 1 h period is marked as −1 h in the graphic representations, to indicate the adsorption−desorption equilibrium. After this period, the solution was irradiated with visible light under stirring. The solution was sampled at t = 0, 5, 15, and 30 min, and after that at 30 min intervals up to 4 h. An UV−vis spectrophotometer was used to analyze the solution samples by monitoring the dye absorbance at 526 nm (λ_{max}). The following formula was used to determine the efficiency of the photocatalytic decolorization:

$$\text{Photocatalytic Efficiency}(\%) = (C_0 - C)/C_0 \times 100 \quad (1)$$

where C_0 is the dye initial concentration, and C is the dye concentration after photoirradiation, which can be estimated by the absorbance at 526 nm using UV−vis spectroscopy. For comparative proposes, the photocatalytic efficiency of the nanocrystalline $Ca_{0.6}Ho_{0.4}MnO_3$ films was further compared with TiO_2 films also produced by sputtering as described in detail elsewhere.[29,30] The catalytic photodegradation experiments were carried out using the procedure aforementioned, using two TiO_2 films with a total area of $19.5\ cm^2$ identical to the $Ca_{0.6}Ho_{0.4}MnO_3$ films.

In order to test the catalysts reuse on fresh dye solutions, the experimental parameters were kept constant, and the photodegradation experiments were repeated for three trials. The same catalysts were used in each photodegradation assay, being washed with distilled water to remove any organic contamination before each run. The structural stability and surface morphology of the photocatalysts were studied by X-ray powder diffraction (XRD), scanning electron microscope (SEM), and diffuse reflectance infrared Fourier transform spectroscopy (DRIFTS) before and after reuse.

2.3. Characterization. The films structural characterization was studied by XRD using a Panalytical X'pert Pro diffractometer ($\theta/2\theta$) equipped with X'Celerator detector and with automatic data acquisition (X'Pert Data Collector (v2.0b) software). The patterns were collected using unfiltered Cu Kα radiation, 40 kV−30 mA, and the Bragg−Brentano geometry over the 2θ range 10−90° with a 2θ-step size of 0.017° and a scan step time of 20 s. The cell parameters were calculated by fitting the observed reflections with a least-squares method, the Checkcell program.[32] The average crystallite size (D) was

evaluated from the XRD data using the Scherrer's equation $D = k\lambda/\beta \cos \theta$, where k is a constant depending on the grain shape (k = 0.89, for circular grain), λ is the wavelength of CuKα radiation, θ is the Bragg diffraction angle of the three most intense peaks ((121), (040) and (123) crystal planes), and β is defined as $\beta^2 = \beta_m^2 - \beta_s^2$, where β_m and β_s are the experimental full width at half maxima (fwhm) and the fwhm of a standard silicon sample, respectively.[33] The microstrain (ε) due to crystal imperfection and distortion developed in manganites films was evaluated from the XRD data, using the relation $\varepsilon = \beta/4tg\theta$.[34]

The scanning electron microscopy (SEM) images were carried out on FEG-SEM JEOL 7001F system operating at 15 keV. In order to prevent charge build up, a thin chromium film was coated on the films surface before the analysis. A JEOL 200CX microscope operating at 300 kV was used to obtain the transmission electron microscopy (TEM) images and selected area electron diffraction (SAED) pattern.

The diffuse reflectance spectra of films were obtained using a UV−vis spectrometer Shimadzu UV-2600PC equipped with an integrating sphere ISR 2600plus over the spectral range 200−900 nm, using $BaSO_4$ reflectance standards. The Kubelka−Munk function, $FKM(R) = (1 − R)^2/2R = K/S$, where K is the absorption and S is the scattering coefficient, was used to analyze the diffuse reflectance spectra.

The absorption of the Rh6G solutions was monitored by an UV−vis spectrophotometer Shimadzu UV-2600, in the range 200−650 nm at a scanning speed of 400 nm min^{-1}.

The diffuse reflection infrared fourier transform spectra (DRIFTS) were collected on a Nicolet 6700 FT-IR attached to Smart Diffuse Reflectance Accessory, in the range of 400−4000 cm^{-1}. The data acquisition was carried out with the program Omnic, and the background was performed with a gold plate.

A commercial water contact angle goniometer (NRL Contact Angle Goniometer, Model 100−00) was used to study the hydrophilic behavior of the films, through the measurement of the water contact angle (CA) on the film surface at room temperature. The CA was measured in four different places, and an average value was estimated for each film.

3. RESULTS AND DISCUSSION

3.1. Catalysts Characterization. The structural characterization of the as-prepared $Ca_{0.6}Ho_{0.4}MnO_3$ films revealed that they are amorphous. The crystallization of the films was attained after annealing at 800 °C during 6 h in air atmosphere. The XRD analysis of the annealed films revealed identical XRD diffraction patterns. In Figure 2 is depicted the representative XRD diffraction pattern for the annealed $Ca_{0.6}Ho_{0.4}MnO_3$ film prepared on fused silica substrate. It can be seen that the film shows a pure typical perovskite structure with no secondary phase formation. Also, the intensity of the peaks relative to the background demonstrates the good crystallinity of the orthorhombic phase. It is obviously seen that all diffraction peaks can be assigned to the crystalline $Ca_{0.6}Ho_{0.4}MnO_3$ powder phase as previously reported[27,35] and can be indexed to a orthorhombic symmetry, space group *Pnma*. The obtained cell parameters (a = 5.4202(4) Å, b = 7.4572(4) Å, c = 5.2926(4) Å, and V = 213.93(4) Å^3) are closely analogous to the ones estimated for powder samples used as sputtering targets and also to the ones that were reported in a previous study by Kobayashi et al.[35]

The average crystallite sizes (D) and the microstrain (ε) for the films were calculated from the peak width at half peak
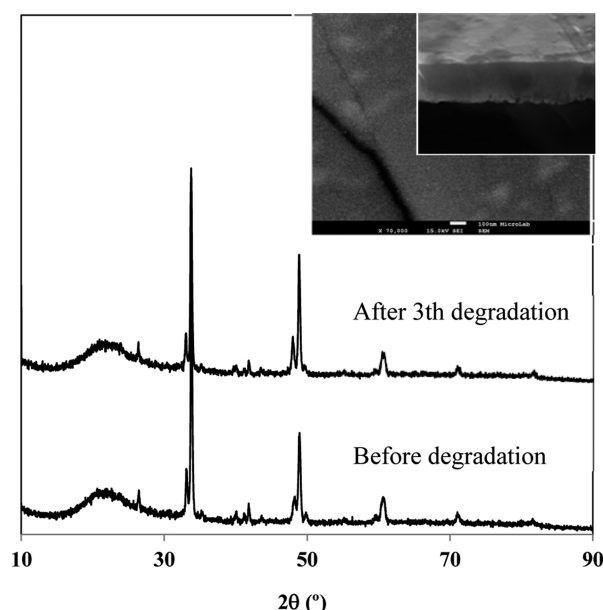
Figure 2. Representative XRD patterns for the $Ca_{0.6}Ho_{0.4}MnO_3$ films before and after three times reuse. Inset: FE-SEM images of the surface and of cross-sectional for the $Ca_{0.6}Ho_{0.4}MnO_3$ films.

height of the three most intense diffraction peaks, based on the instrumental broadening correction. The obtained values for the average crystallite size (D) and for the microstrain (ε) were 33 nm and 1.3047×10^{-3}, respectively. The first value evidences that the nanocrystalline nature of the films and the microstrain value shows that the film exhibits lattice imperfections related to lattice mismatch and thermal mismatch, which can be displayed by some cracks in the films.

The surface morphology of the $Ca_{0.6}Ho_{0.4}MnO_3$ films was analyzed with SEM (inset Figure 2). This technique shows a film with a smooth, dense, and homogeneous surface. It is further observed some cracks at the surface of the film, consistent with the microstrain value estimated by XRD data. It is well-known that the stress in a thin film is originated from intrinsic and extrinsic stresses. The intrinsic stress is associated with defects and impurities. The extrinsic stress is mainly related to lattice mismatch and thermal mismatch.[36] It is also widely known that cracking and spalling of oxide scales and coatings are often caused by thermal stresses, which arise from differential thermal expansion between the substrate and the surface coating. The films present an estimated thickness of approximately 890 nm, which was calculated from the FE-SEM cross-section images (presented as inset of the surface SEM image).

In Figure 3 is presented the representative TEM micrograph for the $Ca_{0.6}Ho_{0.4}MnO_3$ films and the inset shows the corresponding selected area electron diffraction (SAED) pattern. The TEM image and the corresponding SAED pattern show relatively well-defined spots that demonstrate the crystalline nature of the films. This fact is also supported by the XRD results, since the observed peaks intensities in the XRD patterns for the Manganite films are moderately high, as shown in Figure 2. On the other hand, relatively bright electron diffraction rings are also visible in the SAED pattern, revealing that the Manganite films are nanocrystalline.

The band gap energy (E_g) of the $Ca_{0.6}Ho_{0.4}MnO_3$ films was evaluated from the Kubelka−Munk (KM) spectrum (after conversion of diffuse-reflectance to KM) showed in Figure 4, by
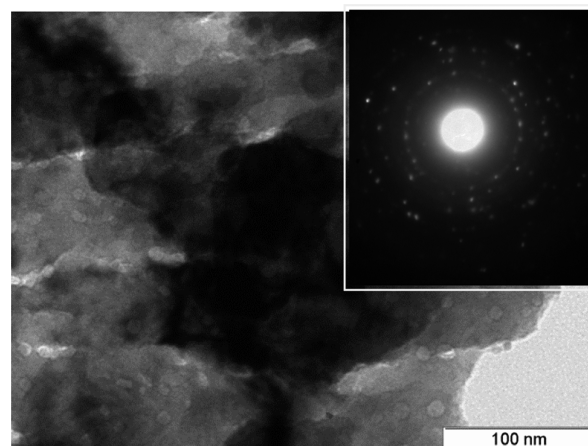
Figure 3. TEM image and SAED pattern for the $Ca_{0.6}Ho_{0.4}MnO_3$ films.
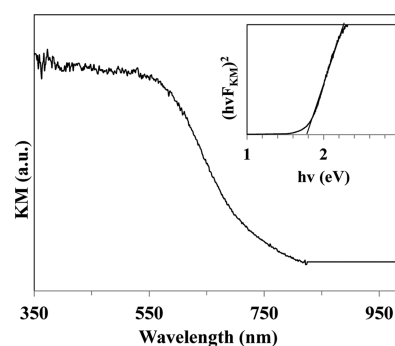
Figure 4. Kubelka−Munk (KM) spectrum (after conversion of diffuse-reflectance to KM) for the $Ca_{0.6}Ho_{0.4}MnO_3$ films. Inset: $(F_{KM} \, h\nu)^2$ versus $h\nu$ for determination of the band gap energy (KM plot).

plotting the function $f_{KM} = (F_{KM} \, h\nu)^2$ versus $h\nu$. The estimated E_g value was 1.8 eV for $Ca_{0.6}Ho_{0.4}MnO_3$ films (inset in Figure 4), and the best fit was found for the direct band gap transition rather than the indirect band gap. In general, for a transition metal oxide with perovskite structure, the band structure is defined by the d level of the transition metal and the O 2p level.[37,38] So the absorption spectra of $Ca_{0.6}Ho_{0.4}MnO_3$ films in the visible light region are controlled by the electronic excitations from O 2p states to Mn 3d states. The calculated E_g value for $Ca_{0.6}Ho_{0.4}MnO_3$ films is red-shifted, and therefore suggests an increase in the number of photogenerated electrons and holes, which can participate in the photocatalytic reaction. This result supports the possibility of using this material as photocatalyst on degradation processes under visible irradiation.

3.2. Photodecolorization Study, Reusability, and Photostability of $Ca_{0.6}Ho_{0.4}MnO_3$ Films.
The photocatalytic activity of $Ca_{0.6}Ho_{0.4}MnO_3$ films was examined by monitoring the degradation of the Rh6G dye. Generally, the photo-oxidation reaction occurs at the catalyst surface; therefore the adsorption characteristics of the catalyst/pollutant system are expected to be key factors on a photocatalytic process. The capability of the $Ca_{0.6}Ho_{0.4}MnO_3$ films to adsorb Rh6G was studied in the absence of light. The experiments did not reveal meaningful evidence of dye adsorption onto the $Ca_{0.6}Ho_{0.4}MnO_3$ films.

The photocatalytic efficiency of the $Ca_{0.6}Ho_{0.4}MnO_3$ films on the decolorization of a 5 ppm Rh6G solution was evaluated for

a period of 4 h. The Rh6G decolorization in the absence of catalyst (photolysis) was also tested.

Figure 5 shows an UV−vis spectra of Rh6G decolorization in the presence of $Ca_{0.6}Ho_{0.4}MnO_3$ catalyst under visible light
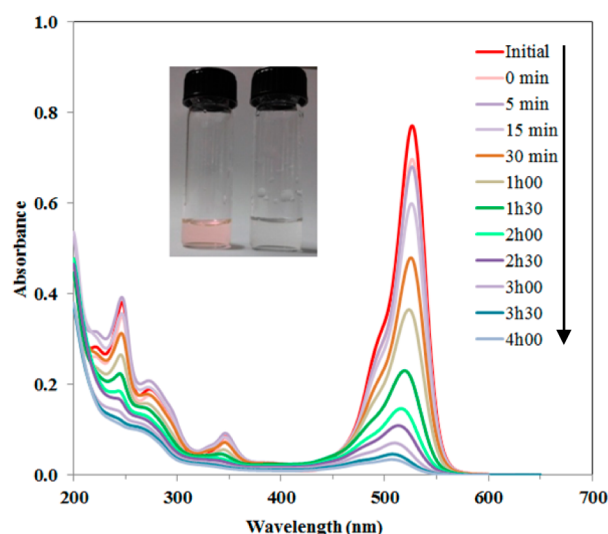
**Figure 5.** UV−vis absorption spectra of Rh6G solution during the first photodegradation experiment, using the $Ca_{0.6}Ho_{0.4}MnO_3$ films as catalyst. Inset is pictorial representation of fresh and decolorized Rh6G.

irradiation. From the analysis of the Rh6G dye spectrum, the three typical Rh6G absorption bands can be observed: the 526 nm band, which correspond to the chromophoric group (the aromatic rings connected by azo groups which are responsible for the dye color) and those at 247 nm and at 275 nm in the UV region, due to the absorption of benzene and naphthalene-like structures in the molecule, respectively.[39] The Rh6G degradation was monitored by measuring the absorbance of the samples taken at regular intervals during a period of 4 h, at the maximum absorption peak of the Rh6G (526 nm).

Under visible irradiation, the films exhibited notable degradation for Rh6G resulting in a decrease in the absorbance at 526 nm, demonstrating that catalytic degradation of the dye occurred during illumination. Also the decrease of the other Rh6G absorption bands with time is in agreement with nearly complete degradation of the dye, i.e., the characteristic absorption peaks of Rh6G decreased with increasing of irradiation time, and finally disappeared, and the solution became colorless.

Figure 6a depicts the Rh6G photodegradation percentage evolution during 4 h of irradiation. For comparison with the catalyst most commonly used, the TiO_2 photocatalyst, degradation assays were carried out with the same experimental conditions using TiO_2 films, namely, the $TiO_2(004)$ films with anatase phase (the label (004) indicates that is observed a preferential growth of the reflection (004) along the c-axis).[7,29,30] In Figure 6a is also plotted the decolorization of a 5 ppm Rh6G solution in the presence of $TiO_2(004)$ films. As can be seen by Figure 6a analysis, the $Ca_{0.6}Ho_{0.4}MnO_3$ films exhibited higher photoactivity for Rh6G dye decolorization in comparison with the TiO_2 films, and therefore were more catalytic in this photodegradation process. In the absence of catalyst, after 4 h of irradiation, 48% of Rh6G degradation was observed. On the other hand, in the presence of the
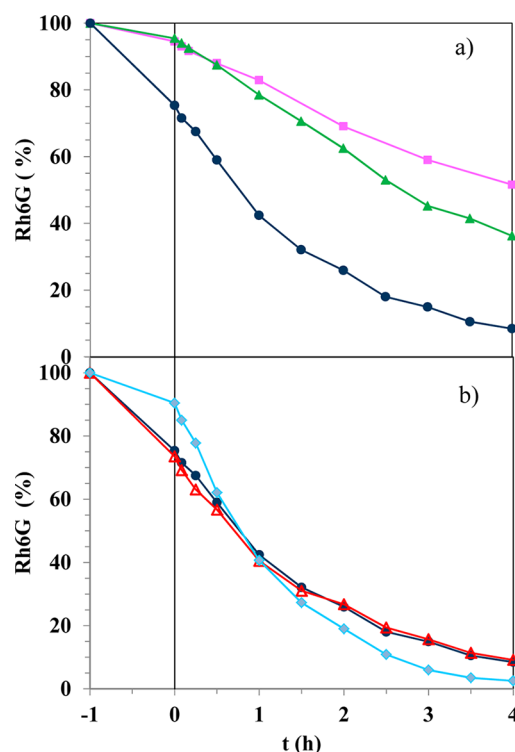
Figure 6. (a) Rh6G degradation percentage evolution during the first photocatalytic degradations of a 5 ppm aqueous solution using $Ca_{0.6}Ho_{0.4}MnO_3$ films (●), $TiO_2(004)$ films (▲), and for photolysis (■); (b) Rh6G degradation percentage evolution during the first (●), second (△) and third (◆) photocatalytic degradations using $Ca_{0.6}Ho_{0.4}MnO_3$ films.

$Ca_{0.6}Ho_{0.4}MnO_3$ or TiO_2 catalysts, only ∼1 h and 2 h 30 min, respectively, were required to degrade the same amount of Rh6G dye. As evident in Figure 6a, after 4 h of visible light irradiation, Rh6G was almost completely degraded when the $Ca_{0.6}Ho_{0.4}MnO_3$ films were used, (92% of dye degradation was observed), while only 64% of dye degradation was detected for the TiO_2 films.

Presently, great efforts have been performed to make the photocatalysis process a good candidate for wastewater treatment. Within this frame and to implement the photocatalytic processes at the industrial scale, it is extremely important to be able to recover and reuse the catalyst, since this will lead to a lower operational cost. In this work, to test the reuse of the same $Ca_{0.6}Ho_{0.4}MnO_3$ catalysts on fresh Rh6G solutions, three successive decolorization experiments were carried out. The obtained results are depicted in Figure 6b.

The analysis of Figure 6b evidence that $Ca_{0.6}Ho_{0.4}MnO_3$ films presents a very good catalytic performance, since only 2% of the initial dye remains in solution after three reuses. In the first degradation trial, 92% of dye was degraded, with a very small change to 91% in the efficiency after two reuses. As compared with the value of 92% obtained after the first assay, an increase of 6.5% in the efficiency after three reuses is observed, since a value of 98% was obtained for Rh6G degradation.

It is well-known that main factors controlling the ABO_3 catalytic performance are the surface area, structural (anionic and cationic) defect density, band structure (band gap) and lattice oxygen activity (related to redox ability of B-site ions). One explanation for the photocatalytic efficiency of the

Manganite films under visible irradiation observed in this work is the band gap energy of $Ca_{0.6}Ho_{0.4}MnO_3$. The estimated band gap energy is 1.8 eV, which indicates a higher reactivity under visible light in comparison with TiO_2 films, which present a wide band gap energy, E_g = 3.27 eV, being more reactive under ultraviolet (UV) light.[7,29] In perovskite type oxides, it is usually considered that A-site cations are catalytically inert components and B-site cations are the catalytically active centers. Therefore, the effect of the A-site cations on photocatalytic process is marginally small when compared with the B-site cations, whose conduction and valence bands principally consist of B 3d orbitals and the O 2p orbitals, respectively.[37,38] Considering the optical band gap (Eg) of the $Ca_{0.6}Ho_{0.4}MnO_3$ films (1.8 eV) and the photocatalytic results, it is revealed that the observed E_g seems to be a ruling factor on those films photocatalytic activity using visible light irradiation. It can also be conclude that manganese-based oxides with perovskite type structures should exhibit high photocatalytic activities in Rh6G photodegradation under visible light irradiation, due to the fact that the formed MnO_6 octahedral chains favor a possible delocalization of charge carriers. The doping with Ho^{3+} can modify the structural defects of the parent perovskite oxide ($CaMnO_3$) and lead to changes in the Mn^{4+}/Mn^{3+} molar ratio. The Mn^{4+}/Mn^{3+} redox couple also plays an essential role in the catalytic action and has a positive influence on the catalytic activity.

The kinetics of photocatalytic degradation of dyes is usually described by the Langmuir−Hinshelwood (LH) kinetic model. The following equation relates the rate of reaction with the dye concentration:

$$r = k_r KC/(1 + KC) \tag{2}$$

where r is the reaction rate, k_r is the reaction rate constant, K is the equilibrium constant, and C is the dye concentration. For a small initial dye concentration (millimolar, i.e., when $KC \ll 1$), this equation can be approximated as a first order process whose rate is given as $r = k_a C$, where k_a is the pseudo-first order reaction rate constant defining the reaction rate .[40]

The concentration of Rh6G dye in aqueous solution tend to decrease exponentially with visible irradiation time, and the photocatalytic decolorization of Rh6G dye can be described by the first-order kinetic model using the following equation:

$$\ln(C_0/C) = k_a t \tag{3}$$

where C_0 and C are the dye initial concentration and its concentration after visible light irradiation for a given time t, respectively. The $\ln(C_0/C)$ of Rh6G is equal to its absorbance values $\ln(A_0/A)$. In Figure 7 are depicted the linear fitted plots of $\ln(A_0/A)$ as a function of visible irradiation time after the three consecutive usages. For comparison, the results for Rh6G photolysis (in the absence of catalyst) and TiO_2 films were also included in Figure 7. The reaction rate constant was achieved using the slope of the line. The calculated correlation constants for the fitted straight lines were R^2 = 0.9984, 0.9977, and 0.9973, and the reaction rate constants of Rh6G photodegradation were 0.5542 h^{-1}, 0.5186 h^{-1}, and 0.9162 h^{-1} for first, second, and third reuse, respectively. The values of R^2 = 0.9949, k = 0.2465 h^{-1}, and R^2 = 0.9990, k = 0.3243 h^{-1} were obtained for TiO_2 films and photolysis assays (without any catalyst), respectively. The degradation of Rh6G dye over $Ca_{0.6}Ho_{0.4}MnO_3$ films was higher than the observed for the immobilized TiO_2 catalyst. On the other hand, the values indicate that decolorization of Rh6G using visible light occurs at a faster rate for the last reuse in comparison with the first and
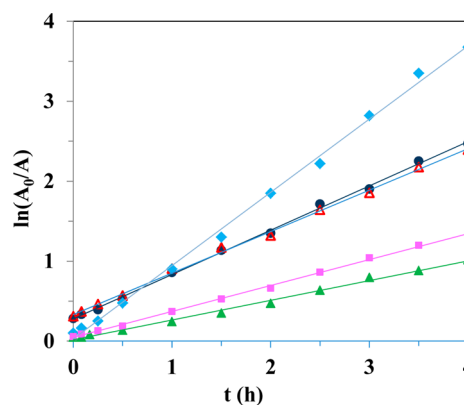
Figure 7. Relationship between $\ln(A_0/A)$ and treatment time. Photolysis (■), $TiO_2(004)$ films (▲), first (●), second (△) and third (◆) photocatalytic degradations using $Ca_{0.6}Ho_{0.4}MnO_3$ films.

second reuses. The kinetic results show an excellent reproducibility, revealing that the films do not deactivate and can be reused after a simple washing.

The $Ca_{0.6}Ho_{0.4}MnO_3$ films' photochemical stabilities were analyzed after photoirradiation. No visible modification on the surface of the films was detected after each photodecolorization run. DRIFTS measurements did not reveal adsorbed organic species on the $Ca_{0.6}Ho_{0.4}MnO_3$ surfaces (Figure 8). Moreover,
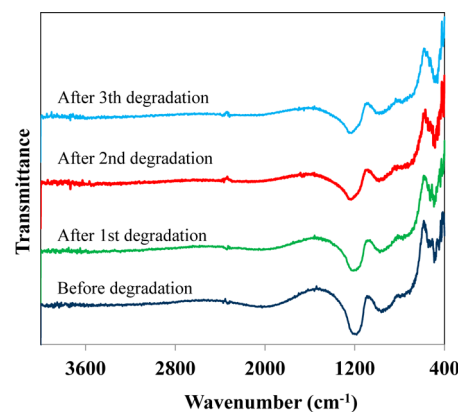
Figure 8. DRIFT spectra for $Ca_{0.6}Ho_{0.4}MnO_3$ films before the photodegradation assays and after reuse three times.

the XRD patterns of the reused $Ca_{0.6}Ho_{0.4}MnO_3$ films matched with the pristine $Ca_{0.6}Ho_{0.4}MnO_3$ (see Figure 2b, where a representative XRD pattern for $Ca_{0.6}Ho_{0.4}MnO_3$ after the third degradation is presented), indicating that $Ca_{0.6}Ho_{0.4}MnO_3$ films are photochemical stable even after reusing them multiple times. The XDR further shows a slight increase on the peaks intensity, which was already described in the literature[41] and is attributed to an increase of the crystallite dimensions as a consequence of the photoirradiation activation process. No modifications on the films surface morphology were detected from the SEM analysis after the reuse (image not shown).

The contact angle (CA) of a liquid drop on a surface is determined by the surface energy and roughness. Wenzel[42] has verified that for a hydrophilic surface (CA < 90°), the increase in roughness leads to an important decrease in CA values. The water contact angle for water droplets on $Ca_{0.6}Ho_{0.4}MnO_3$ films reaches 75°, before and after reuse, signifying that these photocatalysts are still hydrophilic. This result for the contact

angle is in agreement with the SEM analysis for these films, which evidences a smooth surface and therefore a significant CA is expected. The hydrophilic property together with the higher surface area exhibited by the Manganite films facilitates the occurrence of a chemical reaction by the photogenerated holes and electrons and therefore contributes positively to the photodecomposition ability of these materials.

These Manganite films revealed an improvement over titanium dioxide under visible light in the photodegradation of Rh6G, showing a high potential for application as immobilized catalysts in batch or flow photoreactors using solar irradiation. Considering the promising results obtained for the photocatalytic performance and reuse of the Manganite films on the photodecolorization of Rh6G under visible irradiation, the photodegradation of others pollutants in real samples using these materials is currently under progress in our lab.

4. CONCLUSIONS

In this work, $Ca_{0.6}Ho_{0.4}MnO_3$ films were deposited on unheated fused silica substrates by RF-magnetron sputtering using a policrystalline compacted target previously synthesized via the citrate route method at low synthesis temperature. The reuse of nanocrystalline $Ca_{0.6}Ho_{0.4}MnO_3$ films as visible-light photocatalysts was examined on the photocatalytic decolorization of the Rh6G dye. The immobilized $Ca_{0.6}Ho_{0.4}MnO_3$ exhibit a promising catalytic performance in the degradation of Rh6G solutions, under visible light irradiation, without significantly decreasing the removal efficiency after three consecutive usages. We believe that band gap value and the redox ability of the Mn^{4+}/Mn^{3+} couple is a determining factor for the catalytic activity of the Mn-based perovskite oxides. The kinetics of photocatalytic degradation of Rh6G follows a first-order kinetics equation and a higher photocatalytic performance is detected after three reuses. XRD, SEM, and DRIFT evidenced high photochemical stability of the $Ca_{0.6}Ho_{0.4}MnO_3$ films after consecutive photodegradations experiments. These Manganite films revealed an improvement over titanium dioxide under visible light in the photodegradation of Rh6G, showing a high potential for application as immobilized catalysts in batch or flow photoreactors using solar irradiation.

■ AUTHOR INFORMATION

Corresponding Author

*Mailing address: CCMM, Departamento de Química e Bioquímica, Faculdade de Ciências da Universidade de Lisboa, Campo Grande C8, 1749-016 Lisboa. Tel.: +351-21-7500000; Fax: +351-21-7500088; e-mail: mdjorge@fc.ul.pt.

Notes

The authors declare no competing financial interest.

■ ACKNOWLEDGMENTS

■ REFERENCES

(1) Kubacka, A.; Fernandez-García, M.; Colon, G. Advanced Nanoarchitectures for Solar Photocatalytic Applications. *Chem. Rev.* **2012**, *112*, 1555−1614.

(2) Maeda, K.; Domen, K. J. New Non-Oxide Photocatalysts Designed for Overall Water Splitting under Visible Light. *J. Phys. Chem. C* **2007**, *111*, 7851−7861.

(3) Mills, A.; LeHunte, S. J. An Overview of Semiconductor Photocatalysis. *J. Photochem. Photobiol., A* **1997**, *108*, 1−35.

(4) Thuillier, G.; Herse, M.; Labs, D.; Foujols, T.; Peetermans, W.; Gillotay, D.; Simon, P. C.; Mandel, H. The Solar Spectral Irradiance from 200 to 2400 nm as Measured by the Solspec Spectrometer from the Atlas and Eureca Missions. *Sol. Phys.* **2003**, *214*, 1−22.

(5) Thompson, T. L.; Yates, J. T. Surface Science Studies of the Photoactivation of TiO₂ New Photochemical Processes. *Chem. Rev.* **2006**, *106*, 4428−4453.

(6) Diebold, U. The surface science of titanium dioxide. *Surf. Sci. Rep.* **2003**, *48*, 53−229.

(7) Barrocas, B.; Monteiro, O. C.; Melo Jorge, M. E.; Sério, S. Photocatalytic Activity and Reusability Study of Nanocrystalline TiO₂ Films Prepared by Sputtering Technique. *Appl. Surf. Sci.* **2013**, *264*, 111−116.

(8) Varley, J. B.; Janotti, A.; Van de Walle, C. G. Mechanism of Visible-Light Photocatalysis in Nitrogen-Doped TiO₂. *Adv. Mater.* **2011**, *23*, 2343−2347.

(9) Graciani, J.; Nambu, A.; Evans, J.; Rodriguez, J. A.; Sanz, J. F. Au↔N synergy and N-doping of Metal Oxide-Based Photocatalysts. *J. Am. Chem. Soc.* **2008**, *130*, 12056−12063.

(10) Liu, Y.; Son, W.-J.; Lu, J.; Huang, B.; Dai, Y.; Whangbo, M.-H. Composition Dependence of the Photocatalytic Activities of BiOCl$_{1−x}$Br$_x$ Solid Solutions under Visible Light. *Chem.—Eur. J.* **2011**, *17*, 9342−9349.

(11) Wei, W.; Dai, Y.; Yang, K.; Guo, M.; Huang, B. Origin of the Visible Light Absorption of GaN-Rich Ga$_{1−x}$Zn$_x$N$_{1−x}$O$_x$ (x = 0.125) Solid Solution. *J. Phys. Chem. C* **2008**, *112*, 15915−15919.

(12) Zhang, H.; Liang, C.; Liu, J.; Tian, Z.; Wang, G.; Cai, W. Defect-Mediated Formation of Ag Cluster-Doped TiO₂ Nanoparticles for Efficient Photodegradation of Pentachlorophenol. *Langmuir* **2012**, *28*, 3938−3944.

(13) Wei, W.; Dai, Y.; Guo, M.; Zhu, Y.; Huang, B. Density Functional Theory Study of Ag Adsorption on SrTiO₃ (001) Surface. *J. Phys. Chem. C* **2010**, *114*, 10917−10921.

(14) Wang, Z.; Huang, B.; Dai, Y.; Qin, X.; Zhang, X.; Wang, P.; Liu, H.; Yu, J. Highly Photocatalytic ZnO/In₂O₃ Heteronanostructures Synthesized by a Coprecipitation Method. *J. Phys. Chem. C* **2009**, *113*, 4612−4617.

(15) Mu, J.; Chen, B.; Zhang, M.; Guo, Z.; Zhang, P.; Zhang, Z.; Sun, Y.; Shao, C.; Liu, Y. Enhancement of the Visible-Light Photocatalytic Activity of In₂O₃−TiO₂ Nanofiber Heteroarchitectures. *ACS Appl. Mater. Interfaces* **2011**, *4*, 424−430.

(16) Wetchakun, N.; Chaiwichain, S.; Inceesungvorn, B.; Pingmuang, K.; Phanichphant, S.; Minett, A. I.; Chen, J. BiVO₄/CeO₂ Nanocomposites with High Visible-Light-Induced Photocatalytic Activity. *ACS Appl. Mater. Interfaces* **2012**, *4*, 3718−3723.

(17) Defa, W.; Jinhua, Y.; Tetsuya, K.; Takashi, K. Photophysical and Photocatalytic Properties of SrTiO₃ Doped with Cr Cations on Different Sites. *J. Phys. Chem. B* **2006**, *110*, 15824−15830.

(18) Catalan, G.; Scott, J. F. Physics and Applications of Bismuth Ferrite. *Adv. Mater.* **2009**, *21*, 2463−2485.

(19) Gao, F.; Chen, X.; Yin, K.; Dong, S.; Ren, Z.; Yuan, F.; Yu, T.; Zou, Z.; Liu, J. M. Visible-Light Photocatalytic Properties of Weak Magnetic BiFeO₃ Nanoparticles. *Adv. Mater.* **2007**, *19*, 2889−2892.

(20) Parida, K. M.; Reddy, K. H.; Martha, S.; Das, D. P.; Biswal, N. Fabrication of Nanocrystalline LaFeO₃: An Efficient Solegel Auto-Combustion Assisted Visible Light Responsive Photocatalyst for Water Decomposition. *Int. J. Hydrogen Energy* **2010**, *35*, 12161−12168.

(21) Li, S.; Jing, L.; Fu, W.; Yang, L.; Xin, B.; Fu, H. Photoinduced Charge Property of Nanosized Perovskite-Type LaFeO₃ and its

Relationships with Photocatalytic Activity under Visible Irradiation. *Mater. Res. Bull.* **2007**, *42*, 203–212.

(22) Li, F. T.; Liu, Y.; Liu, R. H.; Sun, Z. M.; Zhao, D. S.; Kou, C. G. Preparation of Ca-doped LaFeO$_3$ Nanopowders in a Reverse Microemulsion and their Visible Light Photocatalytic Activity. *Mater. Lett.* **2010**, *64*, 223–225.

(23) Niu, X.; Li, H.; Liu, G. Preparation, Characterization and Photocatalytic Properties of REFeO$_3$ (RE = Sm, Eu, Gd). *J. Mol. Catal. A: Chem.* **2005**, *232*, 89–93.

(24) Li, Y.; Yao, S.; Wen, W.; Xue, L.; Yan, Y. Sol-Gel Combustion Synthesis and Visible-Light-Driven Photocatalytic Property of Perovskite LaNiO$_3$. *J. Alloys Compd.* **2010**, *491*, 560–564.

(25) Wang, S. F.; Yang, H.; Xian, T.; Liu, X. Q. Size-Controlled Synthesis and Photocatalytic Properties of YMnO$_3$ Nanoparticles. *Catal. Commun.* **2011**, *12*, 625–628.

(26) Stafford, U.; Gray, K. A.; Kamat, P. V. Photocatalytic Degradation of Organic contaminants. Halophenols and Related Model Compounds. *Heterogen. Chem. Rev.* **1996**, *3*, 77–104.

(27) Sousa, D.; Nunes, M. R.; Silveira, C.; Matos, I.; Lopes, A. B.; Melo Jorge, M. E. Ca-site Substitution Induced a Metal–Insulator Transition in Manganite CaMnO$_3$. *Mater. Chem. Phys.* **2008**, *109*, 311–319.

(28) Isasi, P. H.; Lopes, M. E.; Nunes, M. R.; Melo Jorge, M. E. Low-Temperature Synthesis of Nanocrystalline Ca$_{1-x}$Ho$_x$MnO$_{3-\delta}$ ($0 \leq x \leq 0.3$) Powders. *J. Phys. Chem. Solids* **2009**, *70*, 405–411.

(29) Sério, S.; Melo Jorge, M. E.; Maneira, M. J. P.; Nunes, Y. Influence of O$_2$ Partial Pressure on the Growth of Nanostructured Anatase Phase TiO$_2$ Thin Films Prepared by DC Reactive Magnetron Sputtering. *Mater. Chem. Phys.* **2011**, *126*, 73–81.

(30) Sério, S.; Melo Jorge, M. E.; Coutinho, M. L.; Hoffmann, S. V.; Limão-Vieira, P.; Nunes, Y. Spectroscopic Studies of Anatase TiO$_2$ Thin Films Prepared by DC Reactive Magnetron Sputtering. *Chem. Phys. Lett.* **2011**, *508*, 71–75.

(31) Franco, A.; Neves, M. C.; Carrott, M. M.; Mendonça, M. H.; Pereira, M. I.; Monteiro, O. C. Photocatalytic Decolorization of Methylene Blue in the Presence of TiO$_2$/ZnS Nanocomposites. *J. Hazard. Mater.* **2009**, *161*, 545–550.

(32) Single Crystal and Powder Diffraction — Freely Available Crystallographic Software for Academia: http://www.ccp14.ac.uk/mirror/mirror.htm.

(33) Cullity, B. D. *Elements of X-ray Diffraction*, 2nd ed.; Addison-Wesley: Reading, MA, 1978.

(34) Guazzone, F.; Payzant, E. A.; Speakman, S. A.; Ma, Y. H. Miscrostrains and Stresses Analysis in Electroless Deposited Thin Pd Films. *Ind. Eng. Chem. Res.* **2006**, *45*, 8145–8153.

(35) Kobayashi, T.; Takizawa, H.; Endo, T.; Sato, T.; Shimada, M.; Taguchi, H.; Nagao, M. Metal-Insulator Transition and Thermoelectric Properties in the System $(R_{1-x}Ca_x)MnO_{3-\delta}$ (R: Tb, Ho, Y). *J. Solid State Chem.* **1991**, *92*, 116–129.

(36) Li, Y. F.; Yao, B.; Lu, Y. M.; Cong, C. X.; Zhang, Z. Z.; Gai, Y. Q.; Zheng, C. J.; Li, B. H.; Wei, Z. P.; Shen, D. Z.; et al. Characterization of Biaxial Stress and its Effect on Optical Properties of ZnO Thin Films. *Appl. Phys. Lett.* **2007**, *91*, 021915-1–021915-3.

(37) Cox, P. A. *Transition Metal Oxides*; Oxford University Press: Oxford, 1992.

(38) Voorhoeve, P. J. H., *Advanced Materials in Catalysis*; Burton, J. J., Garten, R. L., Eds.; Academic Press: New York, 1977.

(39) Bem, V.; Neves, M. C.; Nunes, M. R.; Silvestre, A. J.; Monteiro, O. C. Influence of the Sodium/Proton Replacement on the Structural, Morphological and Photocatalytic Properties of Titanate Nanotubes. *J. Photochem. Photobiol., A* **2012**, *232*, 50–56.

(40) Sivalingam, G.; Nagaveni, K.; Hegde, M. S.; Madras, G. Photocatalytic Degradation of Various Dyes by Combustion Synthesized Nanoanatase TiO$_2$. *Appl. Catal., B* **2003**, *45*, 23–38.

(41) Iskandar, F.; Nandiyanto, A. B. D.; Yun, K. M.; Hogan, C. J., Jr.; Okuyama, K.; Biswas, P. Enhanced Photocatalytic Performance of Brookite TiO$_2$ Macroporous Particles Prepared by Spray Drying with Colloidal Templating. *Adv. Mater.* **2007**, *19*, 1408–1412.

(42) Wenzel, R. N. Surface Roughness and Contact Angle. *J. Phys. Colloid Chem.* **1949**, *53*, 1466–1467.